IOP Publishing | Institute of Physics and Engineering in Medicine Physics in Medicine & Biology

Phys. Med. Biol. **60** (2015) 7543–7566 doi:10.1088/0031-9155/60/19/7543

Dose fractionation in synchrotron radiation x-ray phase micro-tomography

Thibaut Frachon[1,2,4,5], Loriane Weber[1,2], Bernhard Hesse[1,2,3], Simon Rit[1,2], Pei Dong[1,2], Cecile Olivier[1,2], Françoise Peyrin[1,2] and Max Langer[1,2]

[1] European Synchrotron Radiation Facility, 6 rue Jules Horowitz, F-38043 Grenoble Cedex, France
[2] Université de Lyon, CREATIS, CNRS UMR5220, Inserm U1044, INSA-Lyon, Université Lyon 1, 7 avenue Jean Capelle, F-69621 Villeurbanne, France
[3] Julius Wolff Institute & Berlin-Brandenburg School for Regenerative Therapies, Charité—Universitätsmedizin Berlin, Augustenburger Platz 1, D-13353 Berlin, Germany
[4] Currently at Université de Grenoble Alpes, LMGP, CNRS UMR5628, Grenoble Institute of Technology, MINATEC, 3 parvis Louis Néel, 38016 Grenoble Grenoble, France
[5] EVEON SAS, 345 rue Lavoisier, Inovallée, F-38330 Montbonnot Saint-Martin, France

E-mail: max.langer@esrf.fr

Received 5 February 2015, revised 10 April 2015
Accepted for publication 7 May 2015
Published 15 September 2015

Abstract

Phase sensitive x-ray imaging expands the applicability of standard attenuation based techniques by offering several orders of magnitude of increase in sensitivity. Due to the short wavelength, x-ray phase is not directly measurable, but has to be put in evidence by the use of phase contrast techniques. The phase can then be reconstructed from one or several phase contrast images. In this study, we consider synchrotron x-ray phase micro-computed tomography (μCT) based on free space propagation for heterogeneous and strongly absorbing objects. This technique generally relies on acquiring several scans of the sample at different detector distances. It is also generally believed that multi-distance phase μCT needs a higher dose input than single distance phase μCT. The purpose of this work is to study the impact of different means of dose fractionation on the reconstructed image quality. We define different acquistion schemes in multi-distance in-line phase μCT. Previously, the exposure time at each sample-to-detector distance was usually kept the same. Here, we let not only the number of distances vary but also the fraction of exposure time at each distance, the total exposure time being kept constant. Phase retrieval is performed with the mixed approach

algorithm. The reconstructed μCT images are compared in terms of accuracy, precision and resolution. In addition, we also compare the result of dose fractionated multi distance phase μCT to single distance phase μCT using the same total radiation dose. In the multi-distance approach, we find that using different exposure times on each distance improves the image quality in the reconstructed image. Further, we show that, despite having the same total dose delivery, the multi distance imaging method gives better image quality than the single distance method, at the cost of an additional overhead from camera displacements and reference images. We show that by optimizing the acquistion parameters in terms of number of distances and exposure time at each distance, the resulting image quality can be improved. This means that for a desired image quality, a lower radiation dose can be used. This is important especially in high resolution imaging where the radiation dose used for imaging can be very large, potentially damaging the sample. Based on the acquired data, we define an optimal protocol for use in together with the heterogeneous object mixed approach.

Keywords: x-ray imaging, computed tomography, synchrotron radiation, phase contrast, phase tomography, image quality, dose fractionation

(Some figures may appear in colour only in the online journal)

1. Introduction

X-ray computed micro-tomography (μCT) is an important tool in medicine as well as in life science and materials science to characterize samples in 3D. X-ray μCT is based on the acquisition of 2D projections over a range of angles and on 3D reconstruction from the 2D projections. Standard μCT exploits the attenuation of x-rays when they pass through the sample, and when a monochromatic x-ray beam is used, the CT image can be interpreted as a map of the linear attenuation coefficient within the sample. An important drawback of this technique is the lack of sensitivity, especially for soft tissue. This can easily be seen on a standard x-ray radiograph, where hard tissues such as bone are readily visible, whereas contrast in soft tissue such as muscle and tendon is limited.

Phase contrast μCT offers several advantages for the investigation of biological samples compared to standard attenuation μCT (Boistel *et al* 2011, Zanette *et al* 2011). First, phase contrast μCT was shown to be several orders of magnitude more sensitive than standard μCT (Momose and Fukuda 1995). This can be used to visualize fine structures in soft tissue (Guigay *et al* 2007, Horng *et al* 2014). Second, due to this sensitivity, the dose absorbed by the sample can be kept lower than with attenuation based techniques. Several ways to achieve x-ray phase contrast have been presented. In this work, we use free space propagation, known in the literature as in-line phase contrast or propagation based imaging (PBI).

PBI is implemented by letting a highly coherent and monochromatic x-ray beam propagate in free space over a finite distance after interaction with an object to obtain a Fresnel diffraction pattern (Snigirev *et al* 1995). Using these diffraction patterns directly as input to a tomographic reconstruction algorithm yields an edge enhancement effect due to the phase contrast, and is called phase contrast tomography (Cloetens *et al* 1997). Reconstruction of the phase shift from diffraction patterns is called phase retrieval. Several algorithms for phase retrieval from Fresnel diffraction patterns have been developed. Most of these rely on linearization of the Fresnel integral to yield efficient algorithms (Nugent *et al* 1996, Cloetens *et al* 1999,

Guigay *et al* 2007). The resulting phase maps are used to tomographically reconstruct the 3D refractive index distribution, with algorithms such as filtered back projection (FBP) (Cloetens *et al* 1999, Herman 2009).

Two approaches commonly used for phase retrieval from Fresnel diffraction patterns are the Transport of Intensity Equation (TIE) (Teague 1982, Nugent *et al* 1996, Paganin *et al* 2002) and the Contrast Transfer Function (CTF) (Guigay 1977, Cloetens *et al* 1999). The TIE is valid for short object-to-detector distances and the CTF is valid for objects with slowly varying phase and weak absorption. Both approaches can be derived from the squared modulus of the Fresnel transform of the transmittance function (which describes the Fresnel pattern in the case of uniform illumination). Guigay *et al* (2007) showed that the CTF does not approach the TIE in the limit of short distances, and that the TIE does not approach the CTF in the limit of weak attenuation. They proposed an extension to the CTF called the mixed approach, which is valid for slowly varying objects (hence strong absorption is permitted) and approaches the TIE in the limit of short distances, thus reconciling the CTF and the TIE. One particularity of the CTF-based methods is that they allow the use of several phase contrast images taken at different sample-to-detector distances. This allows for a better coverage of the recorded phase information in the frequency domain (Zabler *et al* 2005), at the cost of increased acquisition time (notably camera displacement and extra reference images) and computational load (image registration of the phase contrast images taken at different distances). However, information transfer from phase shift to contrast in the low spatial frequency range is still weak, which makes phase retrieval from Fresnel diffraction patterns sensitive to low frequency noise (Langer *et al* 2010). Several approaches to overcome this limitation have been proposed. Paganin *et al* (2002) introduced a homogeneity criterion on the object in the TIE, thus achieving a single distance phase retrieval algorithm. Object homogeneity has also been used in the CTF based methods, but rather introduced as an *a priori* on the low spatial frequencies of the phase (Langer *et al* 2010). This approach has been extended to multi-material (Langer *et al* 2012a) and heterogeneous objects (Langer *et al* 2014) under the assumption that the sample composition is roughly known.

Dose delivery to the sample is, like in medical imaging, an important problem in x-ray microscopy, albeit for different reasons. Since the dose is inversely proportional to the square of the pixel area (Podgorsak 2005), it can be very high when going towards nanometre resolution (Langer *et al* 2012b). This can become problematic during the imaging, since the high dose absorbed by the sample can cause sample motion or even crack formation. This radiation damage can also change the behaviour of the samples in less directly obvious ways. For example, it has been shown that the mechanical properties of bone can be changed due to the irradiation in x-ray μCT imaging, which creates problems in longitudinal or *in situ* mechanical studies (Barth *et al* 2011). Therefore, in many biomedical imaging problems, it is important to reduce the dose delivered to the sample while keeping the image quality correct.

Due to its high sensitivity, phase contrast imaging makes it possible to reduce the input dose. As outlined above, this can be implemented either by single distance methods (with certain limitations) or multi-distance ones. Experimentally, multi-distance phase μCT has, until now, always been implemented by keeping the same dose at each distance, yielding to a total dose proportional to the number of distances. In this paper, we investigate whether varying the number of distances and the delivered dose at each distance while keeping the same global dose can increase image quality. Since the dose is proportional to the exposure time, all other parameters being fixed, we will express everything in terms of exposure time. Based on the data used here, we define a best protocol in terms of number of distances used and fractions of exposure time on each distance to maximize image quality for a given dose. Conversely, this should allow to minimize dose input for a desired image quality. Further, we

Table 1. Distances and fractions of the total exposure time (0.7 s) used for the reconstructions.

		Distances						
	Dataset	1	2	3	4	5	6	7
Same exposure time at each distance–holotomography	1a	1/7	1/7	1/7	1/7	1/7	1/7	1/7
	1b	1/5		1/5		1/5	1/5	1/5
	1c	1/3		1/3				1/3
	1d	1/2		1/2				
Same total exposure time–holotomography	2a	1/2		1/3				1/7
	2b	1/3		1/5		1/5	1/7	1/7
	2c	1/7	1/7	1/5		1/5		1/3
	2d	1/5		1/3				1/2
	2e	1/5		1/7		1/5	1/7	1/3
	2f	1/5	1/7	1/5	1/7	1/5		
	2g	1/5				1/5		1/2
	2h	1/5		1/5		1/5		1/3
	2i	1/7		1/5		1/5	1/7	1/3
	2j	1/3			1/7			1/2
Single distance–Paganin's algorithm	3a							1
	3b			1				
Attenuation–FBP	4a	1						

Note: The reconstructions are split into four data sets. Dataset 1 corresponds to multi-distance acquisitions with a constant exposure time over each distance. Dataset 2 corresponds to multi-distance acquisitions with varying exposure time for each distance, and varying number of distances, but constant total exposure time. Dataset 3 corresponds to single-distance acquisitions reconstructed using Paganin's algorithm. Dataset 4 is the attenuation acquisition reconstructed with the standard FBP algorithm.

compare the results from the multi-distance reconstructions with single distance reconstructions where the same total imaging dose was used. Presently, single distance phase retrieval algorithms rely on the assumption of a homogeneous object, however. To bridge the gap to the multi-distance approach allowing heterogeneous objects, we also include a homogeneous object multi-distance approach in the comparison.

2. Materials and methods

2.A. Experimental setup

In-line phase contrast tomography was performed at beamline ID19 at the ESRF, Grenoble, France. We used a 'pink beam' mode, the first harmonic of undulator radiation (Pacureanu *et al* 2012). It provides a highly coherent, quasi-monochromatic beam of ~19 keV. For detection, a FReLoN CCD camera (Labiche *et al* 2007) with 2048 × 2048 pixels imaging a scintillating screen using standard light microscope optics was used. An equivalent pixel size of 3.5 μm was chosen. A beam shutter was used during the experiment, so that the x-Ray beam was on the sample only during integration. The dose is then directly proportional to the exposure time. An exposure time of 0.7 s per projection was sufficient to use the full dynamic range of the detector. This exposure time is used as the reference in the following, for example in table 1. We acquired 599 projections per tomographic scan. Each scan also included a dark current image as well as reference images *i.e*. images of the beam without the sample to correct for

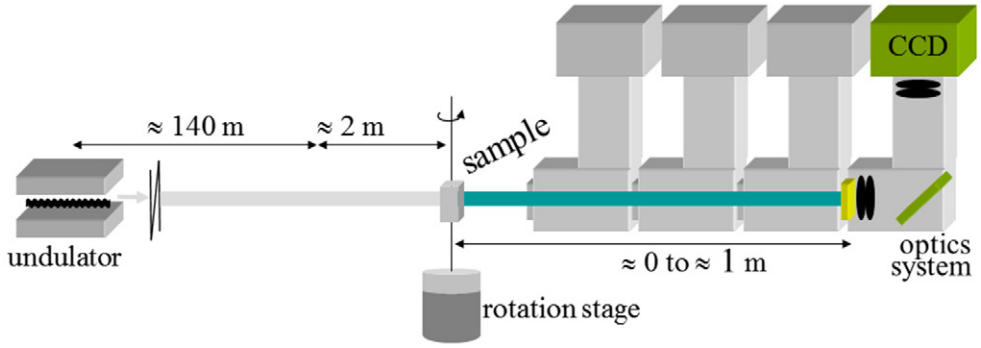

Figure 1. Experimental setup. Unfiltered undulator radiation at ~19 keV x-ray energy is used to perform the imaging. The sample is placed on a rotation stage to perform tomographic imaging. The detector is placed on a translation stage to allow for in-line phase contrast imaging.

beam and detector inhomogeneities. The detector was mounted on a translation stage to allow for different propagation distances of the beam after interaction with the object (figure 1).

2.B. Acquisitions

A phantom object composed of three different wires, one of aluminum, one of magnesium and one of polyethylene terephthalate (PET), was imaged. We performed several acquisitions: one standard attenuation scan using the full dynamic range of the detector, two phase contrast scans at two different distances at full dynamic range to be used for single distance phase retrieval, and four multi-distance acquisitions with different number of distances, where the total counting time was kept identical to the counting time for a full dynamic scan. Due to limited access to beam time, we chose to perform scans consisting of 2, 3, 5 and 7 distances to cover a relatively large range of number of distances.

The choice of distances was made according to Zabler *et al* (2005), where distances are selected based on the zero crossings of the CTF and the optimal contrast for the smallest resolvable feature in the image to yield a combined transfer function for all distances that is as constant as possible. The distances used were D = [100, 200, 280, 580, 897, 950, 1056] mm, referenced below by their number as [1, 2, 3, 4, 5, 6, 7]. The longest and the shortest distance were limited by the beamline instrumentation. Four sets of reconstructions were defined (table 1). The different acquisitions that were tested are defined by the sets of distances/exposure time that were used.

The first set includes four multi-distance acquisitions with a varying number of distances (7, 5, 3 and 2) using the same total exposure time, and the same exposure time at each distance in each acquisition. Set 2 includes ten conditions with varying number of distances constructed from the individual distances in set 1, to achieve multi-distance scans with varying exposure time at each distance, but a close to equal total exposure time to the acquisitions in set 1. The sets 3 and 4 include only one distance and will be used for single distance phase tomography reconstruction and attenuation reconstruction.

2.C. Reconstruction

Reconstructions were performed using three phase retrieval algorithms: the multi-distance mixed approach for homogeneous objects (Langer *et al* 2010), the mixed approach for

heterogeneous objects (Langer *et al* 2014), and the single distance Paganin's method (Paganin *et al* 2002). We outline these methods briefly below.

If we consider a monochromatic, coherent, uniform and parallel x-ray beam, the optical properties of object can be described by its complex refractive index:

$$n(\mathbf{r}) = 1 - \delta_n(\mathbf{r}) - \mathrm{i}\beta(\mathbf{r}) \tag{1}$$

where $\mathbf{r} = (r, s, t)$ are the spatial coordinates in the object domain. The x-ray interaction with the object at each projection angle θ can be described by a transmittance function:

$$T_\theta(\mathbf{x}) = a_\theta(\mathbf{x}) \exp[\mathrm{i}\varphi_\theta(\mathbf{x})] = \exp[-B_\theta(\mathbf{x}) + \mathrm{i}\varphi_\theta(\mathbf{x})] \tag{2}$$

where the attenuation $a_\theta(\mathbf{x})$ and phase shift $\varphi_\theta(\mathbf{x})$ are projections of the real and imaginary parts of $n(\mathbf{r})$ and $\mathbf{x} = (x, y)$ are the spatial coordinates in the transversal plane. Free space propagation over D after interaction with the object can be described by the Fresnel transform with parameter D (Goodman 2005):

$$T_{\theta,D}(\mathbf{x}) = \mathrm{Fr}_D[T_\theta(\mathbf{x})]. \tag{3}$$

The intensity $I_D(\mathbf{x})$ measured on the detector can be calculated by:

$$I_D(\mathbf{x}) = \left|T_{\theta,D}(\mathbf{x})\right|^2 + \gamma(\mathbf{x}) \tag{4}$$

where $\gamma(\mathbf{x})$ accounts for noise and other imperfections in the image (these contributions, however, are not necessarily additive or independent of the object).

2.C.I. Paganin's method. Paganin's method is based on the TIE to model the intensity. A homogeneous object assumption is introduced in the Radon domain by setting the phase directly proportional to the attenuation. This permits phase retrieval from a single distance, albeit restricted to homogeneous objects. This introduces a proportionality constant that is the ratio δ_n/β, a material and energy dependent parameter that has to be chosen for reconstruction. The resulting reconstruction algorithm becomes a linear filter that can be calculated directly in the Fourier domain as (Paganin *et al* 2002):

$$\varphi(\mathbf{x}) = -\frac{\delta_n}{2\beta}\mathrm{In}\left(\mathcal{F}^{-1}\left\{\frac{\mathcal{F}[I_D(\mathbf{x})]}{1 + \frac{\lambda D}{4\pi}\frac{\delta_n}{\beta}\|\mathbf{f}\|^2}\right\}\right) \tag{5}$$

2.C.II. Mixed approach for homogeneous objects. The mixed approach is instead based on the CTF to model the intensity (Wu and Liu 2003, Guigay *et al* 2007). Instead of defining an analytical form for the phase, the phase is retrieved by solving the minimization problem:

$$\hat{\varphi}_\theta(\mathbf{x}) = \arg\min \sum_D \left|\tilde{I}_{\theta,D,\varphi}(\mathbf{x}) - I_{\theta,D}(\mathbf{x})\right|^2 + \alpha\left|\varphi_\theta(\mathbf{x}) - \varphi_{\theta,0}(\mathbf{x})\right|^2 \tag{6}$$

where $\tilde{I}_{\theta,D,\varphi}(\mathbf{x})$ is the intensity calculated using the mixed approach, $I_{\theta,D}(\mathbf{x})$ the measured intensity, α a regularization parameter and $\varphi_{\theta,0}(\mathbf{x})$ is an initial *a priori* known solution. This allows to introduce *a priori* information in a soft manner, its influence being controlled by α. Previously, $\varphi_{\theta,0}(\mathbf{x})$ has been set to 0 (Langer *et al* 2010), which stabilizes the problem in the high spatial frequency range. Due to low information transfer from phase to contrast in the low

Table 2. Theoretical values of μ cm^{-1} and δ/β-ratio for the different materials used, calculated using the Xop software (Sanchez del Rio and Dejus 2004).

	μ	δ/β
PET	0.891	1784
Mg	5.57	343
Al	10.8	268

spatial frequencies, this resulting algorithm is still sensitive to low frequency noise, however (Langer *et al* 2010).

To address the sensitivity to noise in the low spatial frequency range, *a priori* knowledge is introduced, either in the Radon domain (homogeneous assumption) or in the object domain (which allows for heterogeneous objects). A homogeneous object prior can be written, at each angle, as

$$\varphi_{\theta,0}(\mathbf{x}) = f(\mathbf{x}) * \frac{\delta_n}{2\beta} \ln[I_{\theta,0}(\mathbf{x})], \tag{7}$$

where $f(\mathbf{x})$ is a low-pass filter to introduce the prior in the low frequency range only.

2.C.III. Mixed approach for heterogeneous objects. Heterogeneous object priors need to be introduced in the object domain rather than the Radon domain. This is due to that it is in general not possible to separate the contributions from μ and D in the projections. *A priori* phase maps can be generated based on a reconstructed attenuation tomogram ($D = 0$) which gives an estimate $\hat{\mu}(\mathbf{r})$ of $\mu(\mathbf{r})$ (Langer *et al* 2012a), where $\mu = 4\pi\beta/\lambda$. Here, we use a functional relationship between μ and δ/β to construct a map $\mathrm{m}(\mathbf{r})$ of the local δ/β-ratio. Since there is no good empirical relationship for considering the materials in the phantom, we chose to use a linear interpolation between the known δ/β-ratios of the different materials (Langer *et al* 2014). The μ and δ/β-values for the materials used in the paper are shown in table 2. Applying this map to $\widehat{\beta}(\mathbf{r})$ yields a prior estimate of the refractive index decrement distribution in the object as:

$$\delta_0(\mathbf{r}) = \mathrm{m}(\mathbf{r})\widehat{\beta}(\mathbf{r}). \tag{8}$$

Prior estimates of the phase shift at each projection angle are given by generating forward projections as

$$\varphi_{\theta,0}(\mathbf{x}) = -(2\pi/\lambda) \int_{(\theta,\mathbf{x})\ \text{line}} \delta_0(\mathbf{r})\mathrm{d}z. \tag{9}$$

2.C.IV. Combination of propagation distances and exposure time. To let the exposure time vary in the images at different distances while still letting the total exposure time remain approximately equal, we obtained reconstructions from different combinations of images from the different acquisitions. In the first and second sets we used the mixed approach for homogeneous and heterogeneous samples algorithms. The first set contains the reconstructions of the four multi-distance acquisitions, that is to say using the same exposure time at each distance. The second set contains different combinations of number of distances and exposure time at each distance that yield approximately the same total exposure time. The third set contains reconstructions from images at a single distance using the full dynamic of the detector with Paganin's method. The fourth set is the reconstruction of the attenuation scan using standard FBP.

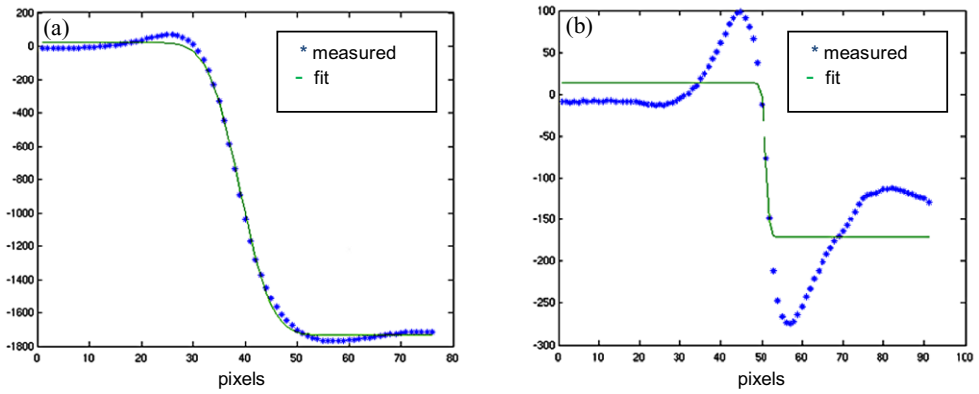

Figure 2. Plot and error function fit across the border of the (a) Al wire in the homogeneous object reconstruction of 2d (figure 6). Material-to-air interface is well reconstructed, and thus a good fit can be obtained. (b) PET wire in the homogeneous object reconstruction 2a (figure 6). The ringing artifact, which is due to the homogeneous object assumption enforcing an inappropriate δ/β-ratio, prevents a good fit.

2.D. Image quality measurement

Quantitative evaluation of the reconstructions was done using the normalized error (NE) of the measured mean density with respect to the theoretical values, the relative standard deviation (RSD) of the measured density with respect to the measured means, and a measure of resolution. These two quantities can be thought of as accuracy and precision, respectively. They are calculated as:

$$\mathrm{NE} = (l_\mathrm{t} - l_\mathrm{m})/l_\mathrm{t}, \ \ \mathrm{RSD} = s_\mathrm{m}/l_\mathrm{m}, \tag{10}$$

where l_m is the measured mean density, l_t is the theoretical density and s_m the measured standard deviation of the density. Resolution was estimated by fitting an error function to a line plot across the edge of each wire (figure 2).

The error function is the primitive function of the Gaussian, which means that the Gaussian parameters can be calculated directly from the error function parameters. The full width at half maximum (FWHM) of the corresponding Gaussian is taken as the resolution estimate. In several reconstructions, strong ringing artifacts, mainly due to the homogeneous object assumption enforcing an incorrect δ/β-ratio, are visible. These artifacts prevent a correct fit and thus a correct resolution measurement (figure 3). Asterisks in tables 3–7 indicates when a correct resolution measurement could not be obtained.

2.E. Verification

After performing all reconstructions in section 2.C. and finding optimal conditions, a phantom of the same composition was imaged at different imaging conditions; once using the standard acquisition scheme (the same exposure time at each distance) with the same number of distances as the optimal scheme, and once using the optimal scheme. For the verification, the phantom was imaged at 0.28 μm pixel size using 19 keV undulator radiation.

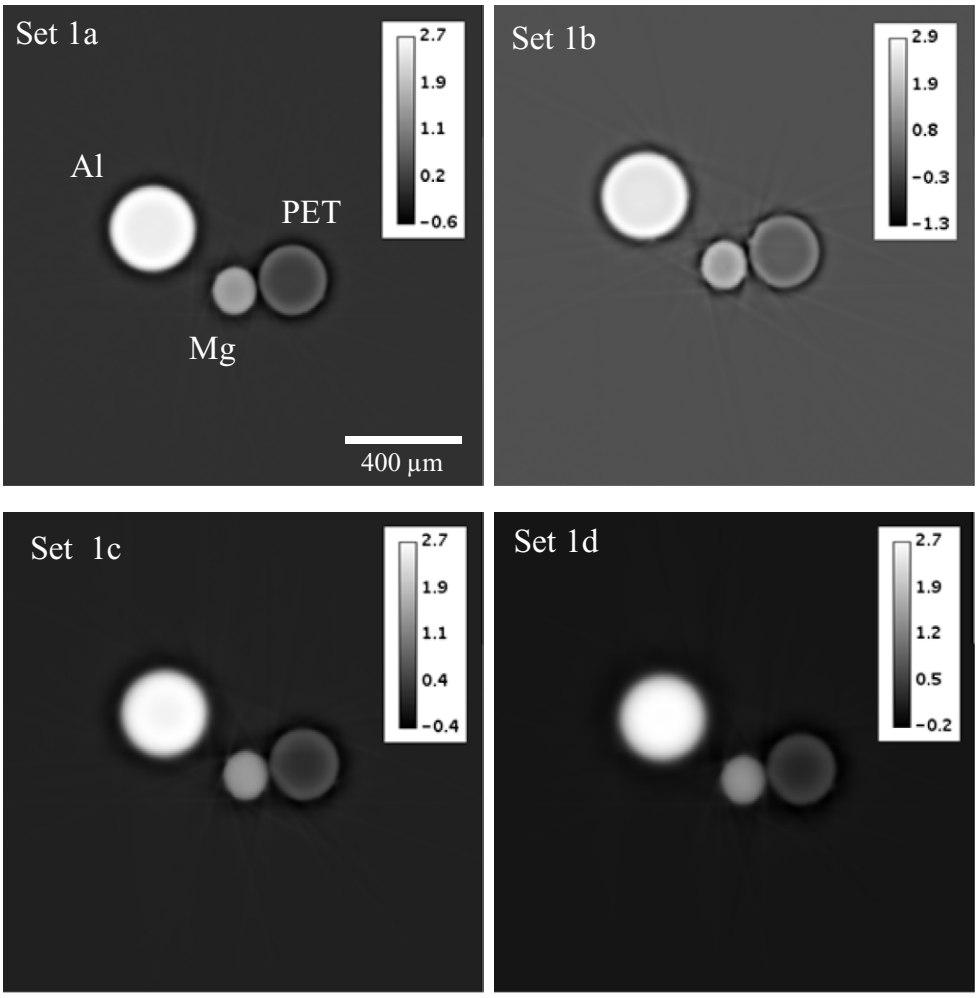

Figure 3. Reconstructed slices of the phantom, consisting of Al, Mg, and PET wires, from set 1 using the homogeneous object mixed approach. The grey level represents mass density. Note that grey levels are not normalized across images but always shows the maximum range present in each image. This is to better show the artifacts present in the images. (1a) 7 distances, (1b) 5 distances, (1c) 3 distances, (1d) 2 distances.

3. Results

3.A. Acquisition set 1 reconstructed with the homogeneous mixed approach

Starting with the reconstructions of set 1 using the mixed approach for homogeneous objects, we can note in the reconstructed slices (figure 4) that ringing artifacts are present on the edges of wires where the chosen δ/β-ratio is poorly adapted. This makes measurement of the resolution impossible in most cases (table 3). Some streak artifacts, reminiscent of beam hardening artifacts, are present in one of the reconstruction (figure 3(1b)). These could be due to beam hardening, since the beam used does not have a very high degree of monochromaticity, but more probably they are due to the incompletely reconstructed phase contrast fringes, which might vary slightly between the projections. Apart from that, it is not

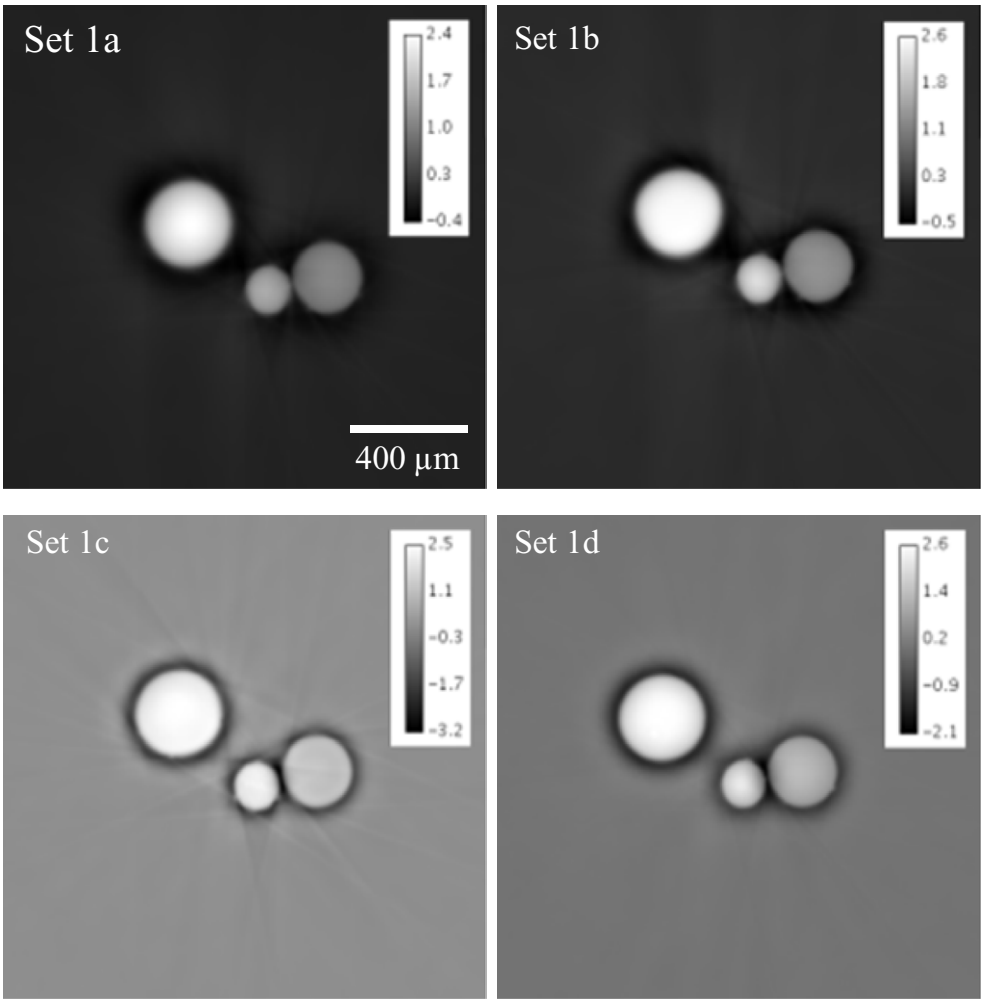

Figure 4. Reconstructed slices from set 1 using the heterogeneous object mixed approach. (1a) 7 distances, (1b) 5 distances, (1c) 3 distances, (1d) 2 distances.

Table 3. Quality measures for set 1 reconstructed using the homogeneous object mixed approach.

	Al			Mg			PET			Average		
	NE (%)	RSD (%)	Resolution (μm)	NE (%)	RSD (%)	Resolution (μm)	NE (%)	RSD (%)	Resolution (μm)	NE (%)	RSD (%)	Resolution (μm)
Set 1a	22.5	0.2	45.2	− 2.8	1.5	29.1	− 75.4	12.8	*	33.5	4.8	*
Set 1b	16.7	0.6	30.8	0.7	0.6	20.6	− 79.0	14.8	*	32.1	5.3	*
Set 1c	16.2	0.3	*	− 6.6	10.1	*	− 78.3	17.6	*	33.7	9.3	*
Set 1d	16.2	0.3	*	− 5.7	1.8	*	− 78.1	5.6	*	33.3	2.6	*

obvious to choose by eye an optimal reconstruction. Also using a quantitative evaluation, choosing best conditions is not straight-forward. Using 7 distances (Set 1a) yields the best result in terms of RSD, while using 3 distances (Set 1c) is best in terms of NE (table 3).

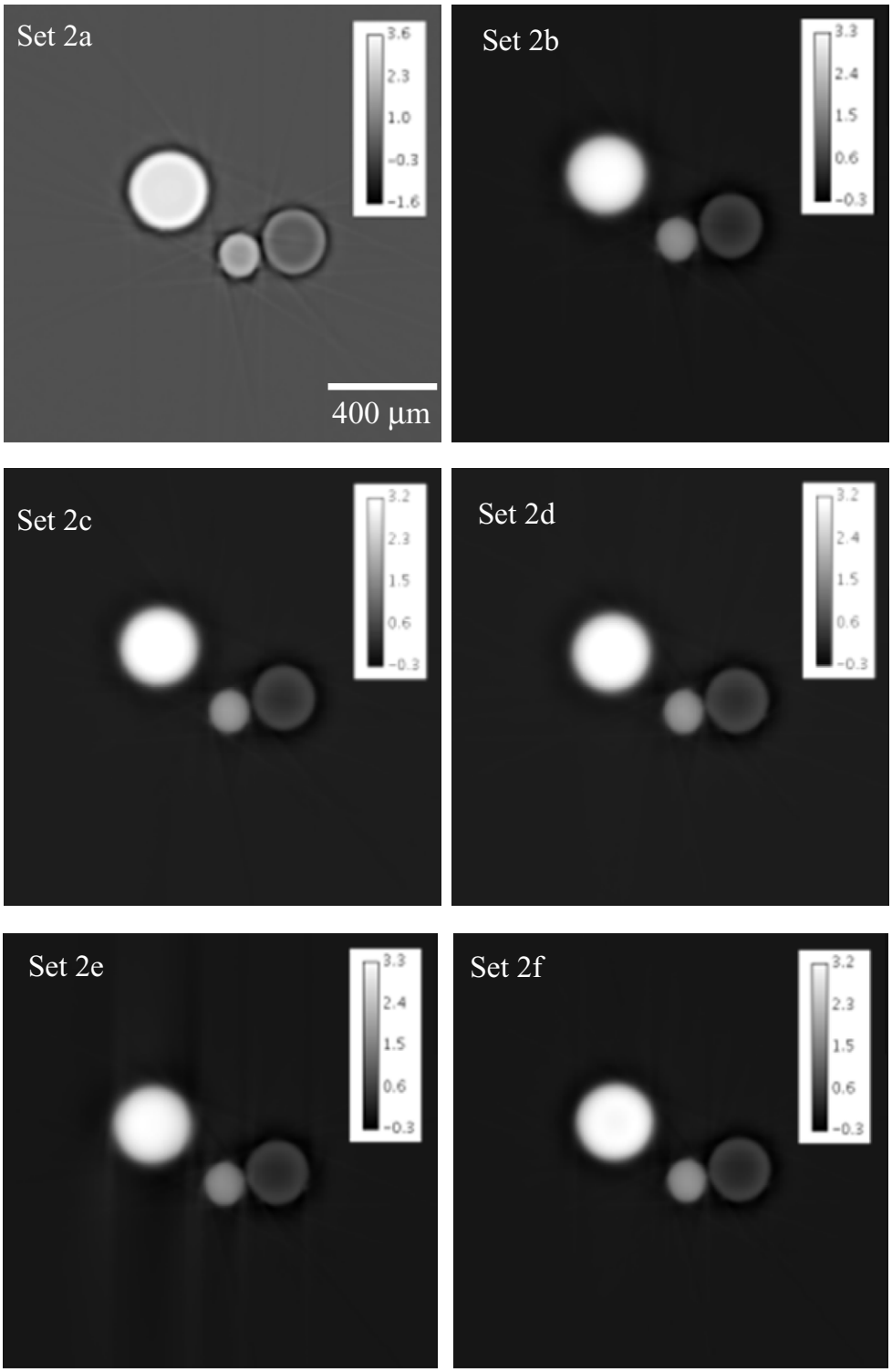

Figure 5. Reconstructed slices from set 2 (constant total exposure time) using the homogeneous object mixed approach.

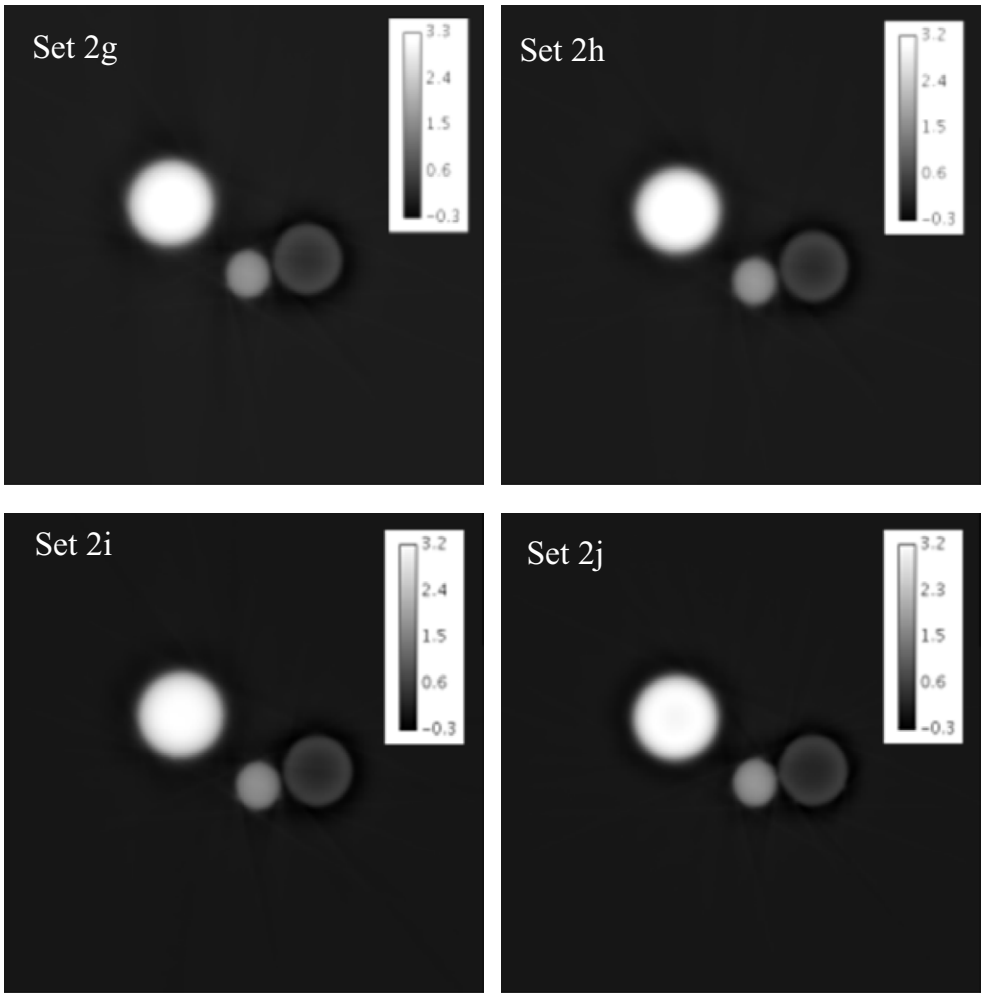

Figure 5. (*Continued*)

3.B. Acquisition set 1 reconstructed with the heterogeneous mixed approach

In contrast to the reconstructions in section 3.A, applying the heterogeneous object prior alleviates the ringing artifacts (figure 5). This makes resolution measurements feasible in more cases (table 4). Reconstructions (1c) and (1d) still shows some ringing artifacts on all interfaces. This is in this case due to some phase contrast being present at the shortest distance. We can note that in the materials where we were able to get a measurement in section 3.A, the resolution seems slightly worse here. On the other hand, both accuracy and precision is substantially improved. The best reconstruction in the set seems to be (1a) (7 distances), despite some overall loss of resolution (mainly in the Al).

3.C. Acquisition set 2 reconstructed with the homogeneous mixed approach

Moving to the reconstructions where we let the exposure time vary between the distances, looking at reconstructions with the homogeneous object prior, we can see that the ringing

Table 4. Quality measures for set 1 reconstructed using the heterogeneous object mixed approach.

	Al			Mg			PET			Average		
	NE (%)	RSD (%)	Resolution (μm)	NE (%)	RSD (%)	Resolution (μm)	NE (%)	RSD (%)	Resolution (μm)	NE (%)	RSD (%)	Resolution (μm)
Set 1a	− 8.5	1.2	49.5	− 15.4	2.5	28.8	3.6	2.5	25.8	9.2	2.1	34.7
Set 1b	− 8.2	0.5	33.4	23.0	3.0	30.6	19.6	1.7	23.2	16.9	1.7	29.1
Set 1c	− 4.3	0.6	*	27.6	2.6	12.2	16.8	4.8	*	16.2	2.7	*
Set 1d	− 0.8	0.2	*	20.8	5.1	22.1	24.6	3.5	*	15.4	2.9	*

artifact is present here as well, for the same reason as in section 3.A (figure 6). Quantitative results are summarized in table 5.

3.D. Acquisition set 2 reconstructed with the heterogeneous mixed approach

Continuing with the heterogeneous object mixed approach reconstructions of the varying exposure time combinations, we can remark a substantial improvement in image quality (figure 7). As opposed to the previous cases, we can now achieve a good resolution measurement in most cases. From table 6 we can see that the best reconstructions are from set 2d and 2e. To decide between them becomes a question of what is desired; 2d is the most accurate, while 2e is more precise and achieves a slightly higher spatial resolution.

3.E. Single distance reconstructions

Finally, we look at the reconstructions from images at one distance, that is the standard attenuation scan and the reconstructions using Paganin's method. In the attenuation tomogram (figure 8), we can see that some phase contrast is present on the edges of all three fibers, and that contrast is relatively weak compared to the phase tomograms. In the single distance phase tomograms, we again see the characteristic ringing artifacts where the chosen δ/β-ratio is far from the physical value. Here, we only show the reconstructions made with the δ/β-ratio (corresponding to Al) that gave the best image quality.

From table 7, we can see that the propagation distance used for the reconstruction does not have a strong impact on the image quality. This is most likely due to that the propagation distances are relatively short with respect to the x-ray energy and detector pixel size. Like the homogeneous mixed approach, Paganin's method yields relatively poor accuracy for a heterogeneous object, due to the homogeneous object assumption. It does yield good precision provided there is enough attenuation in the sample: in the PET fiber for example this is not the case.

3.F. Verification

Based on the results above, the best practicable conditions were deemed to be set 2d. Data were acquired as described in section 2.E corresponding to set 2d and 1c. Phase tomograms were reconstructed using the heterogeneous mixed approach and using Paganin's method on a full dynamic scan as above. The results acquired are fully in line with what was found on the lower resolution data (figure 8). The wide ring artifacts present in these reconstructions are probably due to inhomogeneities in the scintillator being augmented by the intrinsic LF-amplification of the phase retrieval process, in combination with an object that is piecewise constant in cross-section. These artifacts are not very strong from a quantitative point of view, however, as the RSD in these images lies between 4.4% and 7.0%.

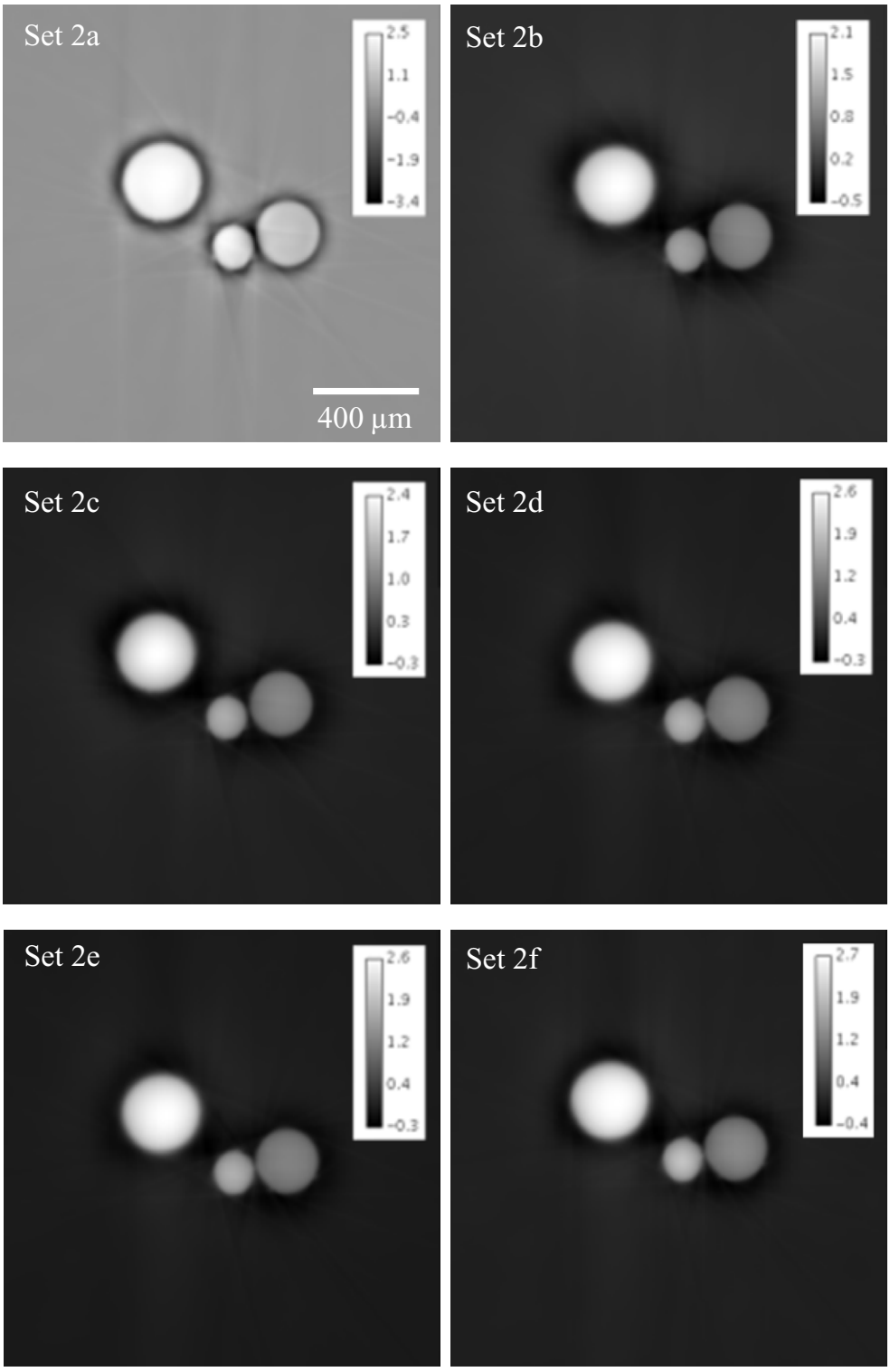

Figure 6. Reconstructed slices from set 2 (constant total exposure time) using the heterogeneous object mixed approach.

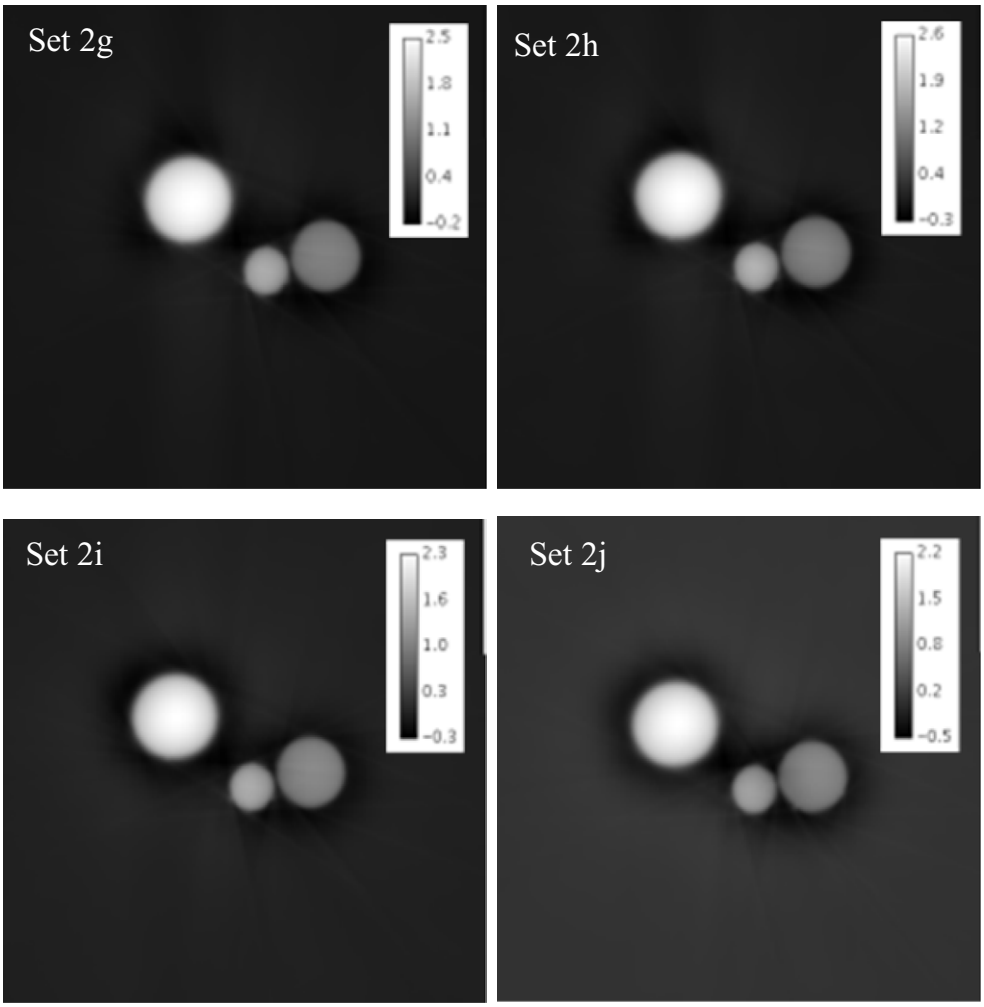

Figure 6. (*Continued*)

4. Discussion

The main aim of this work was to study experimentally the hypothesis often expressed that acquiring images at several distances in in-line phase μCT increases the dose delivered to the sample. The rationale for doing an empirical study is that currently, no realistic simulation of phase μCT exists, i.e. a simulation that takes into account noise sources such as dust on vacuum windows, imperfections in monochromators, to give just two examples. A first important conclusion is that using more distances does not necessarily increase imaging dose. It can rather diminish the dose used for a given image quality, as it has been shown here.

The data presented here is summarised in table 8. We can see that the heterogeneous object mixed approach seems superior with respect to the NE, hence the quality of the reconstruction in a quantitative measurement sense. In terms of RSD, the situation is less clear cut. While the best reconstruction in terms of RSD was made with tho heterogeneous mixed approach, reconstructions with Paganin's method follows closely behind. For the resolution, finally, Paganin's method seems to perform the best.

Table 5. Quality measures from set 2 images reconstructed using variable exposure time acquisition and with the homogeneous mixed approach.

	Al			Mg			PET			Average		
	NE (%)	RSD (%)	Resolution (μm)	NE (%)	RSD (%)	Resolution (μm)	NE (%)	RSD (%)	Resolution (μm)	NE (%)	RSD (%)	Resolution (μm)
Set 2a	16.8	0.3	*	− 9.4	7.6	*	− 77.3	18.5	*	34.5	8.8	*
Set 2b	24.0	0.2	49.7	− 6.3	2.5	28.6	− 72.1	12.6	*	34.1	5.1	*
Set 2c	22.5	0.2	45.4	− 4.9	2.9	27.4	− 72.8	13.9	*	33.4	5.7	*
Set 2d	23.3	0.2	48.3	− 4.3	1.5	29.4	− 74.6	12.4	*	34.1	4.7	*
Set 2e	23.1	0.8	48.7	− 5.8	2.0	27.6	− 73.7	10.8	*	34.2	4.5	*
Set 2f	19.8	0.5	38.2	− 0.6	1.6	27.9	− 76.5	12.7	*	32.3	4.9	*
Set 2g	24.3	0.4	52.3	− 9.8	3.0	27.0	− 69.3	12.5	*	34.5	5.3	*
Set 2h	23.4	0.2	49.8	− 7.3	3.1	30.8	− 71.6	13.2	*	34.1	5.5	*
Set 2i	23.8	0.1	49.2	− 7.0	3.0	28.2	− 71.4	13.4	*	34.0	5.5	*
Set 2j	19.6	0.6	39.3	0.8	1.2	29.0	− 76.6	11.0	*	32.3	4.3	*

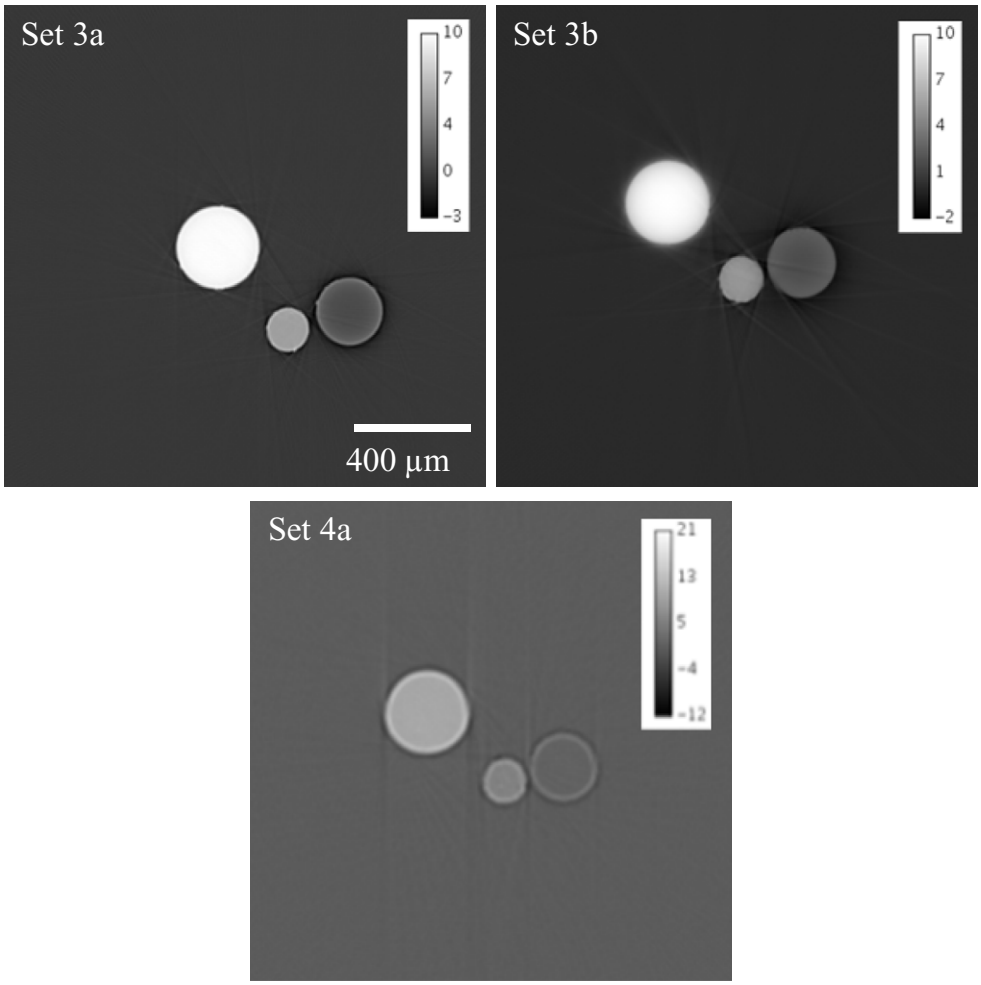

Figure 7. Set 3 (single distance) reconstructed slices with Paganin's method, distance 3 (3a) and 7 (3b), $\delta/\beta = 343$ (grey level representing mass density), and a reconstructed standard FBP (attenuation) slice (4a), grey level representing μ. The streak artefact visible is due to slight sample movement during the acquisition.

Based on the data presented here, we define an optimal acquisition scheme for phase tomography using multi-distance acquisition, valid for these particular conditions. It should be noted that this is not intended as an indication of a general optimal acquisition geometry. It is rather done to demonstrate the possibilities opened by this study, and to give an idea of the magnitude of improvement of image quality that can be expected. In practice, the optimal conditions might be dependent also on parameters of the imaged object. While it is clear that an exhaustive study should be performed, this was not the aim of this work. Further, it is not evident that a general optimal set-up exists. The take-home message should rather be that in dose sensitive applications where time resolved imaging is not the primary goal, using an approach that permits multiple imaging planes might allow to reduce the dose delivered to the samples, and that testing different acquisition schemes in terms of number of distances and exposure time at each distance might allow to further reduce the imaging dose. That stated, we can observe that the most important parameters with respect to the final image quality seem to

Table 6. Quality measures from set 2 images reconstructed using variable exposure time acquisition and with the heterogeneous mixed approach.

	Al			Mg			PET			Average		
	NE (%)	RSD (%)	Resolution (μm)	NE (%)	RSD (%)	Resolution (μm)	NE (%)	RSD (%)	Resolution (μm)	NE (%)	RSD (%)	Resolution (μm)
Set 2a	− 3.7	0.5	15.1	26.4	7.2	11.7	20.2	5.7	*	16.8	4.5	*
Set 2b	− 19.2	1.3	44.0	− 35.5	3.9	23.7	− 15.5	4.0	21.1	23.4	3.1	29.6
Set 2c	− 8.4	1.3	50.2	− 16.9	4.0	26.4	− 4.8	2.3	24.6	10.0	2.5	33.7
Set 2d	− 0.7	1.1	50.6	− 2.3	2.7	34.0	11.5	1.9	27.9	4.8	1.9	37.5
Set 2e	− 1.9	1.1	50.0	− 4.5	2.0	32.8	10.6	1.5	27.2	5.7	1.5	36.7
Set 2f	− 1.2	0.9	44.0	− 8.5	3.3	35.3	17.6	2.2	26.2	9.1	2.1	35.2
Set 2g	− 5.0	1.1	48.1	− 11.6	3.4	27.9	8.8	1.6	25.2	8.5	2.0	33.7
Set 2h	− 1.2	1.1	49.9	− 5.5	4.3	30.5	12.1	2.2	26.0	6.3	2.5	35.5
Set 2i	− 13.2	1.1	45.5	− 20.7	3.4	26.4	2.3	1.9	24.6	12.1	2.1	32.2
Set 2j	− 18.2	1.1	44.7	− 35.2	3.5	25.5	− 16.0	4.2	22.3	23.1	2.9	30.9

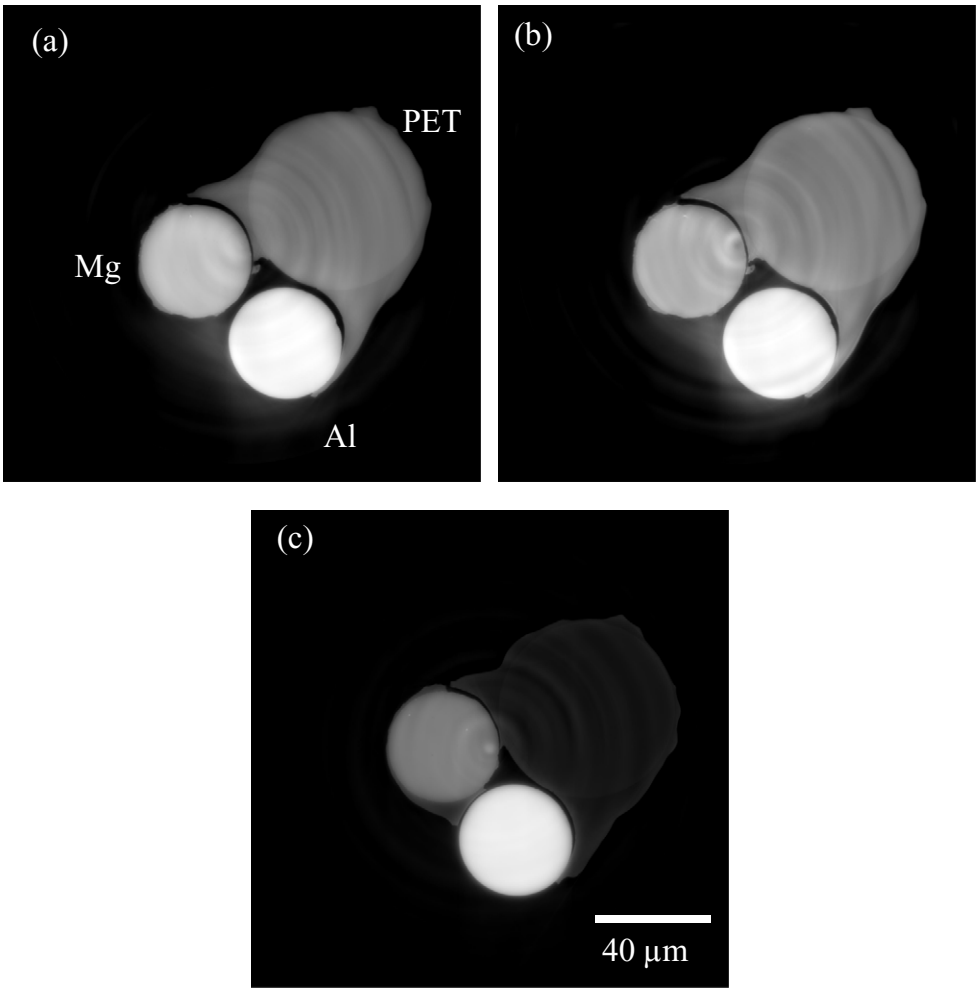

Figure 8. Reconstructions of the verification data: (a) using set 1c and the homogeneous mixed approach (NE: 12.3%, RSD: 4.7%), (b) using set 2d and the heterogeneous mixed approach (NE: 5.9%, RSD: 4.4%), and (c) using Paganin's method (NE: 36.0%, RSD: 7.0%)).

Table 7. Quality measures for single distance reconstructions (attenuation and Paganin's method).

	Al			Mg			PET			Average		
	NE (%)	RSD (%)	Resolution (μm)	NE (%)	RSD (%)	Resolution (μm)	NE (%)	RSD (%)	Resolution (μm)	NE (%)	RSD (%)	Resolution (μm)
Set 3a	15.3	0.1	17.8	− 7.4	0.7	9.7	70.1	4.5	0.7	30.9	1.8	9.4
Set 3b	15.7	0.1	19.5	− 7.4	0.5	12.9	69.7	4.5	4.5	30.9	1.7	12.3
Set 4a	10.1	3.4	*	11.5	9.9	*	188.9	57.0	*	70.2	23.5	*

be first the exposure time in the shortest (in this case the attenuation) distance, and second the exposure time in the longest distance. In terms of image quality, reconstruction 2d and 2e are roughly equivalent. We chose reconstruction 2d because the use of 3 distances is more practical since it limits the overhead from camera displacements.

Table 8. Summary of the results.

	Reconstruction								
	NE			RSD			Resolution		
Dataset	Hom	Het	Pag	Hom	Het	Pag	Hom	Het	Pag
1a					+		*		
1b							*	+++	
1c							*	*	
1d					++++		*	*	
2a							*	*	
2b							*	++	
2c							*		
2d		+++++			++		*		
2e		++++			+++++		*		
2f		+			+		*		
2g		++					*		
2h		+++					*		
2i					+		*		
2j							*	+	
3a						+++			+++++
3b						++++			++++
4a									*

+++++ indicates the best reconstruction for each measurement.

++++ the second best and so on.

* Indicates where it was not possible to obtain a good measurement. Combinations of data sets and methods that do not have an associated reconstruction are greyed out.

To summarize the improvement that can be expected, we can see that the best reconstructions with equal exposure time at east distance achieved an average NE of 9.2% and a RSD of 1.7% respectively (table 4), and the best reconstructions with variable exposure time achieved a NE of 4.8% and a RSD of 1.5%. This corresponds to a potential improvement in accuracy of 48% and an improvement of precision of 12%. Incidentally, the attenuation scan performed good for relatively absorbing materials, and worse and worse for increasingly light materials. In the best case, we achieved a NE of 10.1% and a RSD of 3.4%, both in the Al, and in the worst case, in the PMMA, a NE of 188.9% and a RSD of 57%. This illustrates well the increase in sensitivity of phase-based methods compared to attenuation-based ones.

The imaging conditions we optimized here were how many distances to use and what exposure time to choose at each distance. We did not look at which physical distances to use, but rather followed the results in Zabler *et al* (2005). It seems, however, that to gain a good reconstruction quality one needs at least one phase contrast image at a relatively short distance to have good quality in hard structures, and one phase contrast image at a relatively long distance to achieve good quality in less dense structures.

It can be noted that the total exposure time is not exactly equivalent in all the combinations. None of the quality measures seem to show a strong correlation with total exposure time,

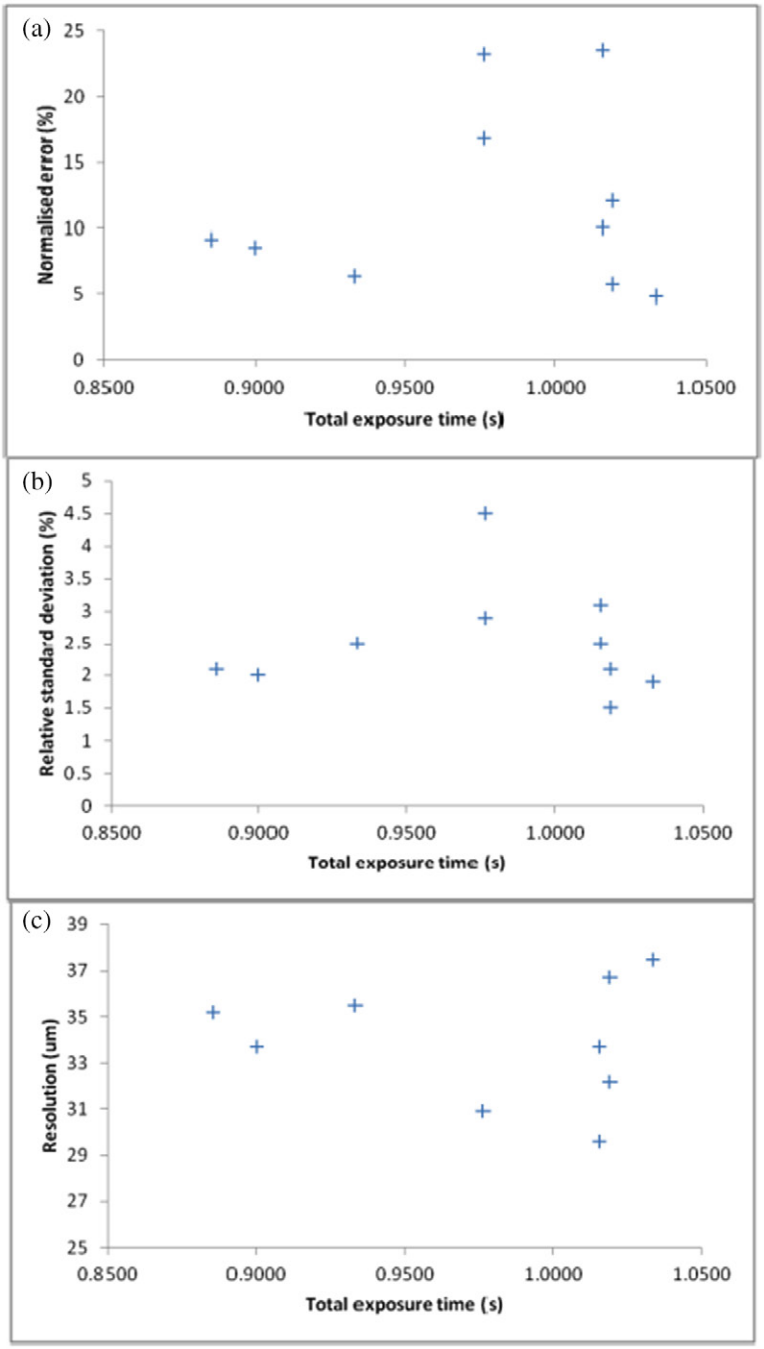

Figure 9. Scatter plot of the three quality measurements against the total exposure time for each reconstruction. Each point represents a reconstruction. (a) NE as a function of the total exposure time, (b) RSD as a function of the total exposure time, (c) resolution as a function of the total exposure time.

however, as can be seen in figure 9, where the different quality measures are plotted against the total exposure time.

One limitation of this study was the resolution measurement. The main problem for resolution measurement with the proposed method is when there are remaining fringe artifacts in the images. These are most often due to incompletely reconstructed phase, usually due to a too low δ/β-ratio. These artifacts increase the error function slope that represents the transition between background and wire. The brighter the fringe, the sharper the slope and the better is the apparent resolution measurement, and at some point, when the fringe is too strong, a good fit is not achieved. Therefore, when analyzing the quality measurements, we put more consideration on precision and accuracy. This can be further motivated by that the better the accuracy and precision, the better different deconvolution or sharpening approaches should work to compensate for the loss of resolution.

Further, we did not study the lower limit of contrast in the phase contrast images. This could be an important parameter to consider, especially for implementation of phase tomography on laboratory type sources. Finally, we did not investigate the influence of using longer distances. There are indications that using longer propagation distances might improve image quality. This could be of particular interest at synchrotron radiation facilities, where flux, coherence, and, more practically, space is less limited.

Finally, this work presents a mainly empirical study. Work has been done in theoretical, numerical, and experimental analysis of noise in phase contrast (Chou and Anastasio 2009, Diemoz *et al* 2012, Majidi *et al* 2014) and phase tomography (Chou and Anastasio 2010). The main result of this work was to demonstrate that improved image quality and reduced delivered dose can be achieved by using a different exposure time at each distance. Concepts from the above theoretical analyses could be applicable to the present case to better understand the results presented here, however, and a more thorough experimental investigation would be needed to define a possibly optimal setup.

5. Conclusion

The main aim of this study was to investigate whether the use of several imaging distances in in-line phase μCT leads to higher imaging dose on the sample. We performed reconstructions based on the standard acquisition scheme, where exposure time is equal at all distances, and with different exposure times at each distance. We also performed reconstructions using a single distance phase retrieval approach. In all the acquisitions, the total exposure time was kept close to constant. We showed that for an equal dose delivery, a multi-distance approach actually yields better image quality than a single distance one. Therefore, the dose delivery is not necessarily higher with the multi-distance approach, contrary to what is commonly believed, but can actually be reduced for a desired image quality. This comes at the cost of additional time for overhead, i.e. moving the camera and taking reference images, however. Further, we found that an appropriate use of different exposure time on each distance can yield an even higher image quality for the same imaging dose, thus further lowering the imaging dose for a desired image quality. In this experiment, we found that 3 distances, with exposure times of 1/5 of the total on the shortest (attenuation distance, followed by 1/3 and 1/2 for the longer distances) yielded the best image quality. It should be noted that the precise fractions could be dependent on resolution, x-ray energy and sample composition. Further, there is most probably a minimum SNR necessary in the images. These aspects are outside the scope of the present study, but clearly merit further investigation. Finally, these results indicate that multi-distance

approaches could be valuable for dose sensitive imaging applications e.g. native state bone or cell imaging, since they can require lower total dose input to achieve the same image quality as with a single distance approach.

Acknowledgments

This work was supported by the LABEX PRIMES (ANR-11-LABX-0063) of Université de Lyon, within the program 'Investissements d'Avenir' (ANR-11-IDEX-0007) operated by the French National Research Agency (ANR).

References

Barth H D, Zimmermann E A, Schaible E, Tang S Y, Alliston T and Ritchie R O 2011 Characterization of the effects of x-ray irradiation on the hierarchical structure and mechanical properties of human cortical bone *Biomaterials* **32** 8892–904

Boistel R *et al* 2011 Whispering to the deaf: communication by a frog without external vocal sac or tympanum in noisy environments *PLoS One* **6** e22080

Chou C-Y and Anastasio M A 2009 Influence of imaging geometry on noise texture in quantitative in-line x-ray phase-contrast imaging *Opt. Express* **17** 14466

Chou C-Y and Anastasio M A 2010 Noise texture and signal detectability in propagation-based x-ray phase-contrast tomography *Med. Phys.* **37** 270–81

Cloetens P, Ludwig W, Baruchel J, Van Dyck D, Van Landuyt J, Guigay J P and Schlenker M 1999 Holotomography: quantitative phase tomography with micrometer resolution using hard synchrotron radiation x rays *Appl. Phys. Lett.* **75** 2912

Cloetens P, Pateyron-Salomé M, Buffière J Y, Peix G, Baruchel J, Peyrin F and Schlenker M 1997 Observation of microstructure and damage in materials by phase sensitive radiography and tomography *J. Appl. Phys.* **81** 5878–86

Diemoz P C, Bravin A, Langer M and Coan P 2012 Analytical and experimental determination of signal-to-noise ratio and figure of merit in three phase-contrast imaging techniques *Opt. Express* **20** 27670–90

Goodman J W 2005 *Introduction to Fourier Optics* 3rd edn (Greenwood Village, CO: Roberts & Company)

Guigay J-P 1977 Fourier transform analysis of Fresnel diffraction patterns and in-line holograms *Optik* **49** 121–5

Guigay J P, Langer M, Boistel R and Cloetens P 2007 Mixed contrast transfer and transport of intensity approach for phase retrieval in the Fresnel region *Opt. Lett.* **32** 1617–9

Herman G T 2009 *Fundamentals of Computerized Tomography* (London: Springer)

Horng A *et al* 2014 Cartilage and soft tissue imaging using x-rays: propagation-based phase-contrast computed tomography of the human knee in comparison with clinical imaging techniques and histology *Invest. Radiol.* **49** 627–34

Labiche J-C *et al* 2007 Invited article: the fast readout low noise camera as a versatile x-ray detector for time resolved dispersive extended x-ray absorption fine structure and diffraction studies of dynamic problems in materials science, chemistry, and catalysis *Rev. Sci. Instrum.* **78** 091301

Langer M, Cloetens P, Hesse B, Suhonen H, Pacureanu A, Raum K and Peyrin F 2014 Priors for x-ray in-line phase tomography of heterogeneous objects *Phil. Trans.* A **372** 20130129

Langer M, Cloetens P, Pacureanu A and Peyrin F 2012a X-ray in-line phase tomography of multimaterial objects *Opt. Lett*. **37** 2151–3

Langer M, Pacureanu A, Suhonen H, Grimal Q, Cloetens P and Peyrin F 2012b X-ray phase nanotomography resolves the 3D human bone ultrastructure *PLoS One* **7** e35691

Langer M, Cloetens P and Peyrin F 2010 Regularization of phase retrieval with phase-attenuation duality prior for 3D holotomography *IEEE Trans. Image Process*. **19** 2428–36

Majidi K, Li J, Muehleman C and Brankov J G 2014 Noise and analyzer-crystal angular position analysis for analyzer-based phase-contrast imaging *Phys. Med. Biol.* **59** 1877–97

Momose A and Fukuda J 1995 Phase-contrast radiographs of nonstained rat cerebellar specimen *Med. Phys.* **22** 375–9

Nugent K, Gureyev T, Cookson D D, Paganin D and Barnea Z 1996 Quantitative phase imaging using hard x rays *Phys. Rev. Lett.* **77** 2961–4

Pacureanu A, Langer M, Boller E, Tafforeau P and Peyrin F F 2012 Nanoscale imaging of the bone cell network with synchrotron x-ray tomography: optimization of acquisition setup *Med. Phys.* **39** 2229–38

Paganin D, Mayo S C, Gureyev T E, Miller P R and Wilkins S W 2002 Simultaneous phase and amplitude extraction from a single defocused image of a homogeneous object *J. Microsc.* **206** 33–40

Podgorsak E B 2005 *Radiation Oncology Physics: a Handbook for Teachers and Students* (Vienna: International Atomic Energy Agency)

Sanchez del Rio M and Dejus R J 2004 Status of XOP: an x-ray optics software toolkit *Proc. SPIE* **5536** 171–4

Snigirev A, Snigireva I, Kohn V, Kuznetsov S and Schelokov I 1995 On the possibilities of x-ray phase contrast microimaging by coherent high-energy synchrotron radiation *Rev. Sci. Instrum.* **66** 5486

Teague M R 1982. Irradiance moments: their propagation and use for unique retrieval of phase *J. Opt. Soc. Am.* **72** 1199

Wu X and Liu H 2003 A general theoretical formalism for x-ray phase contrast imaging *J. X-Ray Sci. Technol.* **11** 33–42 (PMID: 22388096)

Zabler S, Cloetens P, Guigay J-P, Baruchel J and Schlenker M 2005 Optimization of phase contrast imaging using hard x rays *Rev. Sci. Instrum.* **76** 073705

Zanette I, Weitkamp T, Lang S, Langer M, Mohr J, David C and Baruchel J 2011 Quantitative phase and absorption tomography with an x-ray grating interferometer and synchrotron radiation *Phys. Status Solidi* A **208** 2526–32